



Photonic-crystal-enhanced fluorescence: Template-free gold cryosoret nanoassembly steering, dequenching, and augmenting the quenched emission from radiating dipoles

Seemesh Bhaskar,[†] Leyang Liu,[†] Weinan Liu, Joseph Tibbs, and Brian T. Cunningham*

Accepted: 16 December 2024

Photonic-crystal-enhanced fluorescence (PCEF) has emerged as a versatile tool for medical diagnostics and analyte quantification. However, challenges with regard to low sensitivity, experimental artifacts, and negligible emission output in the “zone of inactivity” due to the quenching from plasmonic gold (Au) nanoparticles have remained a major bottleneck. Here, we report the distinct functionalities rendered by hybridizing the PC interface with the Au cryosoret nanoassemblies to not only dequench the quenched emission from radiating dipoles, but also yield augmented 200-fold steering fluorescence output. The performance of the platform is evaluated numerically using rigorous coupled-wave analysis (RCWA) and COMSOL Multiphysics simulations presenting good overlap with the experimentally obtained fluorescence signal, validating the radiating guided mode resonance model. Our approach incorporating the cryosoret nanoassemblies with three-dimensionally distributed nanogaps provides a method to realize integrated and abundant hot spots with insights into material interface engineering and potential applications for biosensing.

Introduction

The ever-growing necessity of augmented sensitivity of various luminescence-based point-of-care (POC) diagnostic technologies dictates the need for improvement of the performance of the associated photonic platforms using effective nanoengineering

methodologies.^{1,2} An appropriate consideration to drastically alter the response of the luminescent moieties is explicitly dependent on the nature of the local micro-nanoenvironment.^{3,4} The interfacial interaction between such moieties and plasmonic nanomaterials, coupled with spectroscopic

Impact statement

Although surface plasmon-coupled emission (SPCE) technology has emerged as a resourceful tool for biosensing applications, it suffers from fundamental dissipative ohmic losses encountered with the underlying metal thin-film substrates. Challenges with regard to low sensitivity, experimental artifacts, and consequent negligible emission output in the “zone of inactivity” due to the quenching from plasmonic gold (Au) nanoparticles have remained a major bottleneck. In order to address this drawback, in this article, we demonstrate rational design, fabrication, and tunability of the lossless guided-mode resonance (GMR) of grating photonic crystals (PCs) to effectuate unprecedented steering fluorescence output that is not only dequenched, but also augmented. The synergistic approach utilizing the polarization selectivity of the PC and the hottest plasmonic hot spots of the Au cryosoret nanoassemblies presented newer insights from a materials engineering perspective substantiating the inferences from experiments (fluorescence) and simulations (RCWA). While the SPCE presented ~10-fold fluorescence enhancement, a ~200-fold enhancement in the photonic-crystal-coupled-enhanced steering (PCEs) emission is demonstrated for identical conditions using the delocalized Bragg plasmons and localized Mie plasmons of the cryosorets fabricated via adiabatic cooling technology. We believe that this quench-free technology will lay the stepping stone for next-gen photoplasmonic devices for chem-biosensing applications.

Seemesh Bhaskar, Department of Electrical and Computer Engineering, University of Illinois at Urbana-Champaign, Urbana, USA; Nick Holonyak Jr. Micro and Nanotechnology Laboratory, University of Illinois at Urbana-Champaign, Urbana, USA; Carl R. Woese Institute for Genomic Biology, University of Illinois at Urbana-Champaign, Urbana, USA

Leyang Liu, Department of Electrical and Computer Engineering, University of Illinois at Urbana-Champaign, Urbana, USA; Nick Holonyak Jr. Micro and Nanotechnology Laboratory, University of Illinois at Urbana-Champaign, Urbana, USA

Weinan Liu, Department of Electrical and Computer Engineering, University of Illinois at Urbana-Champaign, Urbana, USA; Nick Holonyak Jr. Micro and Nanotechnology Laboratory, University of Illinois at Urbana-Champaign, Urbana, USA

Joseph Tibbs, Nick Holonyak Jr. Micro and Nanotechnology Laboratory, University of Illinois at Urbana-Champaign, Urbana, USA; Department of Bioengineering, University of Illinois at Urbana-Champaign, Urbana, USA

Brian T. Cunningham, Department of Electrical and Computer Engineering, University of Illinois at Urbana-Champaign, Urbana, USA; Nick Holonyak Jr. Micro and Nanotechnology Laboratory, University of Illinois at Urbana-Champaign, Urbana, USA; Department of Bioengineering, University of Illinois at Urbana-Champaign, Urbana, USA; Carl R. Woese Institute for Genomic Biology, University of Illinois at Urbana-Champaign, Urbana, USA; Department of Chemistry, University of Illinois at Urbana-Champaign, Urbana, USA; Cancer Center at Illinois, Urbana, USA; bcunning@illinois.edu

*Corresponding author

[†] Seemesh Bhaskar and Leyang Liu contributed equally to this work.

doi:10.1557/s43577-024-00850-2



tools, has emerged as “plasmon-enhanced spectroscopy” know-how with applications in the interdisciplinary fields of single-molecule detection, immunoassays, forensics, food safety evaluation, and molecular diagnostics to name a few.^{5–7} Frontier areas of substrate development in this regard have been focused toward subwavelength electromagnetic (EM) field confinement, tuning and evaluation of the photoplasmonic response using nanomaterials of different sizes, shapes, and inherent materials properties.^{8,9} The thorough engineering of the scattering and absorption cross sections of the plasmonic nanoparticles (NPs) in the vicinity of luminescent moieties has enabled the observation of novel phenomena such as an induced plasmon effect of plasmon-enhanced fluorescence (PEF),^{10,11} Purcell effect,¹² plasmon-soliton¹³ and plasmon-exciton coupling,⁸ Rabi splitting,¹⁴ and Fano resonance.¹⁵ Among several types of plasmonic NPs (Ag, Pt, Pd, Cu, Al, Au, Ni) that are being investigated for modulating the PEF, gold NPs stand out because of unique optical, electronic, and chemical properties, enabling biocompatible physicochemical functionalization in robust configurations for multidisciplinary research.^{16,17} The elevated charge densities of $\approx 5.90 \times 10^{16} \text{ m}^{-3}$ in gold have been utilized for numerous applications where the near-field and far-field radiation patterns from proximal luminescent moieties are being significantly modified for myriad-biosensing applications.^{18–20}

Although a rich spectrum of biomedical applications has been reported with the use of AuNPs, the quenching effects rendered because of the interband ohmic losses in them have remained a long-standing challenge.^{21–24} The large nonradiative channels fostered by higher-ordered plasmonic modes in AuNPs result in the so-called “zone of inactivity” in the spatial regime of $< 5 \text{ nm}$, where the quenching effects are dominant.^{21,25–27} Consequently, different approaches have been developed in the past decade to overcome such undesirable quenching effects, some prominent ones being (1) demonstration of inter-plasmon mixing in advanced superimposed plasmonic modes,²⁸ (2) core-shell architectures with an effective spacer nanolayer,²⁹ (3) anisotropic plasmonic AuNPs supporting sharp protrusions with extreme EM-field intensity,³⁰ and (4) metal-dielectric and heterometallic hybrid nanoarchitectures obtained via complex synthetic protocols.²⁴ Importantly, it has been observed that although the plasmonic NPs with sharp nanogeometries can aid 2–3 orders of magnitude higher field intensity, this is outweighed by the performance of the nanogap antennas in nanoassemblies that can enhance the field intensity by 3–5 orders of magnitude.³¹ Essentially, nanogap antennas *vis-à-vis* pristine NPs assist in the realization of nanogap-driven radiative decay channels, which in turn, boost the quantum yield of the proximal luminophores, hence, establishing the “quenching the quenched” phenomena.^{21,23,32} Kneipp et al. demonstrated the occurrence of “hottest hot spots” where 10^{14} -fold enhancement in the SERS signal intensity was demonstrated using nanoassemblies supporting single-molecule detection.^{33,34} The associated FDTD simulations solving the Maxwell equations yielded 2500

times augmented electric-field intensity for nanoassemblies compared to pristine NPs.^{35,36} Iterative optimization based on algorithms for increasing number of NPs (from 3 to 20) in an assembly has shown promising insights.^{26,35} The field intensity in such plasmonic hot spots monotonically increases with increasing the number of NPs per assembly, not only in the vicinity of the hot spots, but also in the entire ambient nanoenvironment of the nanoassembly. Interestingly, the disordered or anisotropic nanoassemblies have proved to outperform (fivefold better) the linear arrangement of NPs (in a chain format) with regard to the electric-field enhancement.³⁷ The multiplicative enhancement because of the cascading effect in nanoassemblies increases the local electric field at the hottest spot, also called a “nanofocus,” from 580 (trimers) to 1023 (pentamers) to 2500 (hexamers).^{26,37} While the simulations have provided convincing validation in this regard, several experimental tools such as electron energy-loss spectroscopy (EELS) imaging and SERS have confirmed the formation and performance of such hottest hot spots in nanoassemblies.^{38,39} In light of these observations, although there are different approaches that are being developed for synthesis of nanoassemblies, their applicability for biosensing and related applications is hampered on account of the multistep template dependent, processes, long synthetic time intervals, laborious methodology, and expensive chemical reagents.^{40–42} In this background, there is an increasing requirement for designing innovative approaches to overcome the quenching effects encountered with AuNPs, where nanoassemblies obtained via cost-effective methods are to be employed to realize dequenching for photonics-based sensing applications.

In this article, we design such quintessential template-free cryosoret nanoassemblies using AuNPs by subjecting the colloidal AuNPs to adiabatic cooling.^{43,44} Further, the synthesized cryosorets are interfaced with the guided mode resonance (GMR) of a PC to generate hottest hot spots thereby addressing the previously mentioned quandary (i.e., need for using AuNPs because of its utility in biomedical research and the simultaneous objective to overcome the quenching encountered in AuNPs).^{45–47} Through this report, we present the simulations (RCWA and COMSOL) and experimental PC-enhanced fluorescence (PCEF) results with an excellent overlap between them, demonstrating the utility of Au cryosorets (AuCSs) in dequenching the quenched emission in addition to steering the emission with 200-fold enhancement in the signal intensity compared to detecting fluorescent emission from the same nanostructures on a glass interface. While the pristine AuNPs presented quenched ~ 10 -fold emission enhancements, AuCSs yielded dequenched and augmented emission. Moreover, here we present newer insights into the radiating GMR model (using simulations) proposed in our recent work,⁴⁸ by thorough investigation of the emission pattern of the radiating dipoles in near field at the PC interface, validating the experimentally observed steering/beaming fluorescence output, also termed as PC-enhanced



steering (PCES) emission. Recently, there is a growing interest in obtaining large-area, far-field, and directional fluorescence output using resonant microcavities and PC-based substrates.^{49–51} The high steering fluorescence enhancements reported here through cryosoret nanoengineering would support a paradigm shift in adopting newer nanosynthesis approaches for realizing high EM-field hot spots supporting robust biosensing platforms toward translational and convergent research.

Experiment and simulation

A conceptual schematic of the optical framework utilized to collect the experimental fluorescence is presented in **Figure 1a**. All the PC substrates were cleaned with piranha solution (4:1 ratio of H_2SO_4 and H_2O_2 solutions) and rinsed with acetone, IPA, and Milli-Q water before use. The radiating dipoles (rhodamine B) were evenly distributed over the PC substrate using a well-established spin-coating method.^{48,52} Two percent PVA polymer spin-coated at 3000 rpm for 1 min yielded ~65-nm thin films (degree of hydrolysis 86–89%; molecular weight 85,000–12,000 and 4000 g/mol), and additional details are presented in our earlier work.⁴⁸ All the PC substrates utilized for experimentally measuring the fluorescence were fabricated by embedding the radiating dipoles in the polymer matrix. Further, they are mounted on a calibrated 360° rotating stage, with optical configuration shown in **Figure 1a**. This configuration can be visualized as a reverse Kretschmann configuration without a prism,^{53–55} from the perspective of surface plasmon resonance (SPR). Consequently, as the laser is directly exciting the dye and the emission from the dye is outcoupled through the PC, we have termed this phenomenon as photonic-crystal-coupled emission (PCCE), in line with earlier works (PCCE is a subclassification of the broad field of PCEF).^{56,57} A 532-nm cw laser is aligned using appropriate mirrors and incident at the PC surface from the free space side, via the iris and collimating lens (**Figure 1a**). So as to present direct comparisons with the experimentally obtained fluorescence enhancements of earlier works in the domain of surface plasmon-coupled emission (SPCE) and PCCE,^{48,58} we have used rhodamine B (fluorescent reporter) as the radiating dipole, across all the measurements in this work. The outcoupled emission is collected using a 550-nm long-wave pass (LWP) filter, and a fiber-optic (coupled to collimating lens) spectrometer (2000+) connected to Ocean Optics SpectraSuite software. The functionality of different PC variants (of different GMR) with the rhodamine B and 532-nm laser source is comprehensively evaluated in our recent work where the PCES emission platform was established.⁴⁸ In order to understand the polarization selectivity response of the underlying PC substrates, we have used an input polarizer (P1) and output polarizer (P2) in accordance with our earlier work.⁴⁸ A sheet polarizer (P1) was used to excite the PC substrate using one of the polarizations of the laser beam. A sheet polarizer (P2) was used in vertical and horizontal orientations to collect the TM- and TE-polarized

emission by placing it between the PC substrate and the detector. The PC interface that presents the GMR overlapping with that of the emission of the radiating dipoles yielded the best performance, and the same was utilized in the current work, in order to make conclusive remarks.

The Turkevich technique was used for the synthesis of AuNPs.^{26,58,59} **Figure 1b** displays the conceptual scheme for the steps involved in the synthesis of the cryosoret nanoassembly. Freshly made aliquots of AuNPs colloidal aqueous solutions were collected and subjected to an adiabatic chilling chamber (containing liquid nitrogen, LN2) using glass vials. The glass vial had a capacity of 10 mL and a diameter of 25 mm. The vials containing NPs were submerged in liquid N_2 (LN2) at -196°C and taken out at predetermined intervals. Following our previously reported protocol,^{44,45} the samples were taken out at predetermined intervals (15, 30 s, 1, 2, 3 min) and thawed back to room temperature without being stirred. The cryosoret nanoassembly method is a temperature-driven, external stimuli-based method that enables an easy, fast, and cost-effective method of obtaining robust nanoassemblies.^{19,44,45} Thus, obtained AuCSs are well characterized using JEOL 2100 CRYO transmission electron microscopy (TEM) and the TEM images of cryosorets obtained by subjecting the AuNPs to LN2 for 15, 30 s, 1, 2, and 3 min are shown in **Figure 1c–h**, respectively, and these samples are consecutively labeled as S1–S5 in the subsequent sections for simplicity. From the TEM characterization, it is observed that with increase in the time of adiabatic cooling, the number of nanoparticles per assembly increases, thereby presenting a larger number of plasmonic hot spots (due to nanovoids and nanocrevices).

Numerical simulations were performed by rigorous coupled-wave analysis (RCWA) to obtain the dispersion diagram of the PC under consideration (that showed sharp transverse electric [TE] resonance at 575-nm wavelength, which is the emission wavelength of the radiating dipole).⁴⁸ The simulated response of the PC was computed for normal illumination of TE-polarized light (polarization parallel to grating lines). The fabrication details of the PC used for all the simulation and experimental measurements are presented in our earlier work.⁴⁸ The transmittance modes (emerging from GMR) sustained by the PC obtained via simulations were overlapped with the experimentally obtained fluorescence data to understand the system from a physics point of view. Further, simulation results on the near-field pattern and far-field radiation of a radiating dipole with and without cryosorets were performed using different orientations of the dipole over the PC using RF module COMSOL Multiphysics simulations for the electric-field component.

Results and discussion

The optical schematic utilized in all the experimental work resembles the RK configuration without the prism.⁵⁵ In our recent work, we demonstrated steering fluorescence output by matching the fluorescence emission signal maximum to

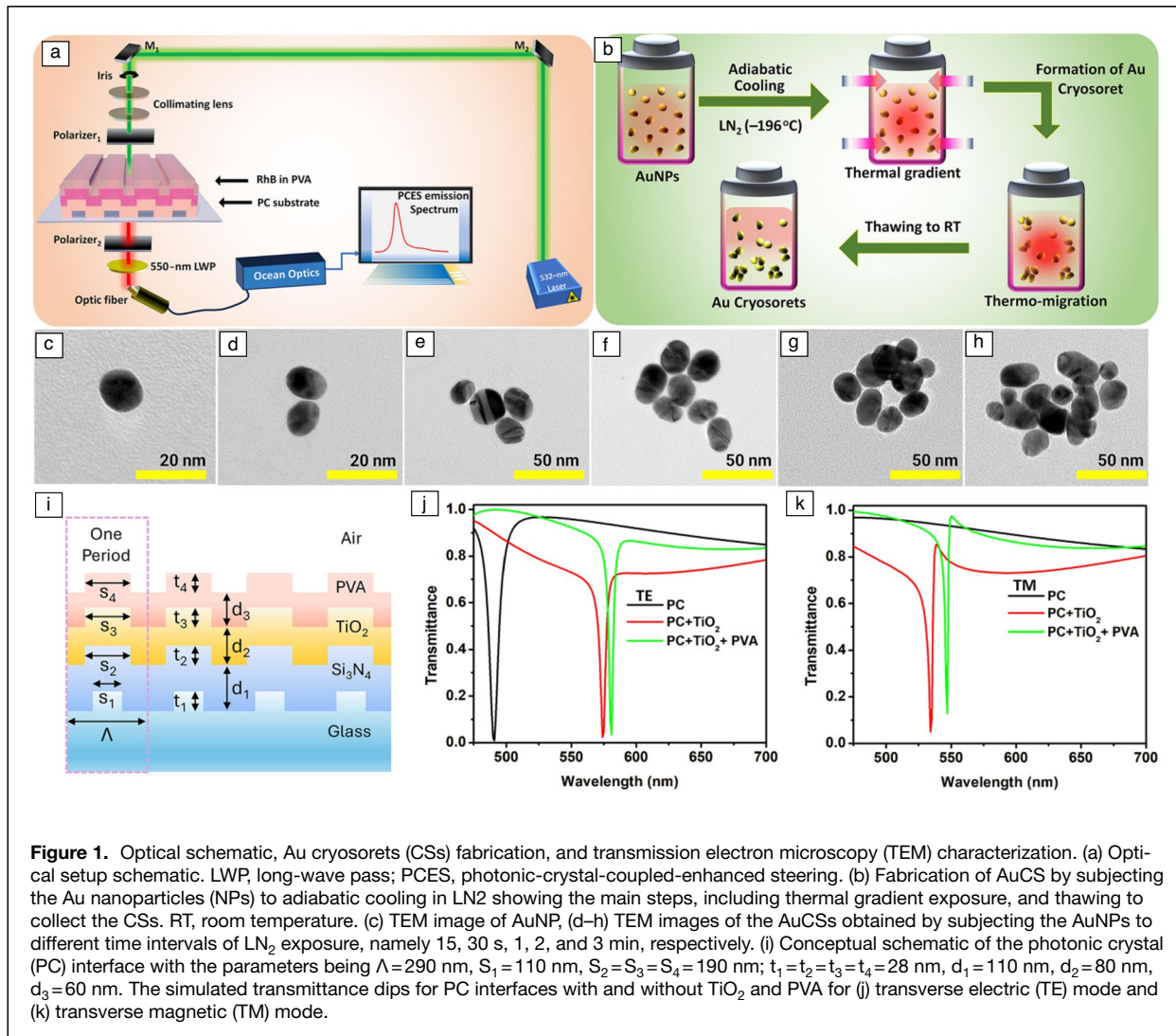


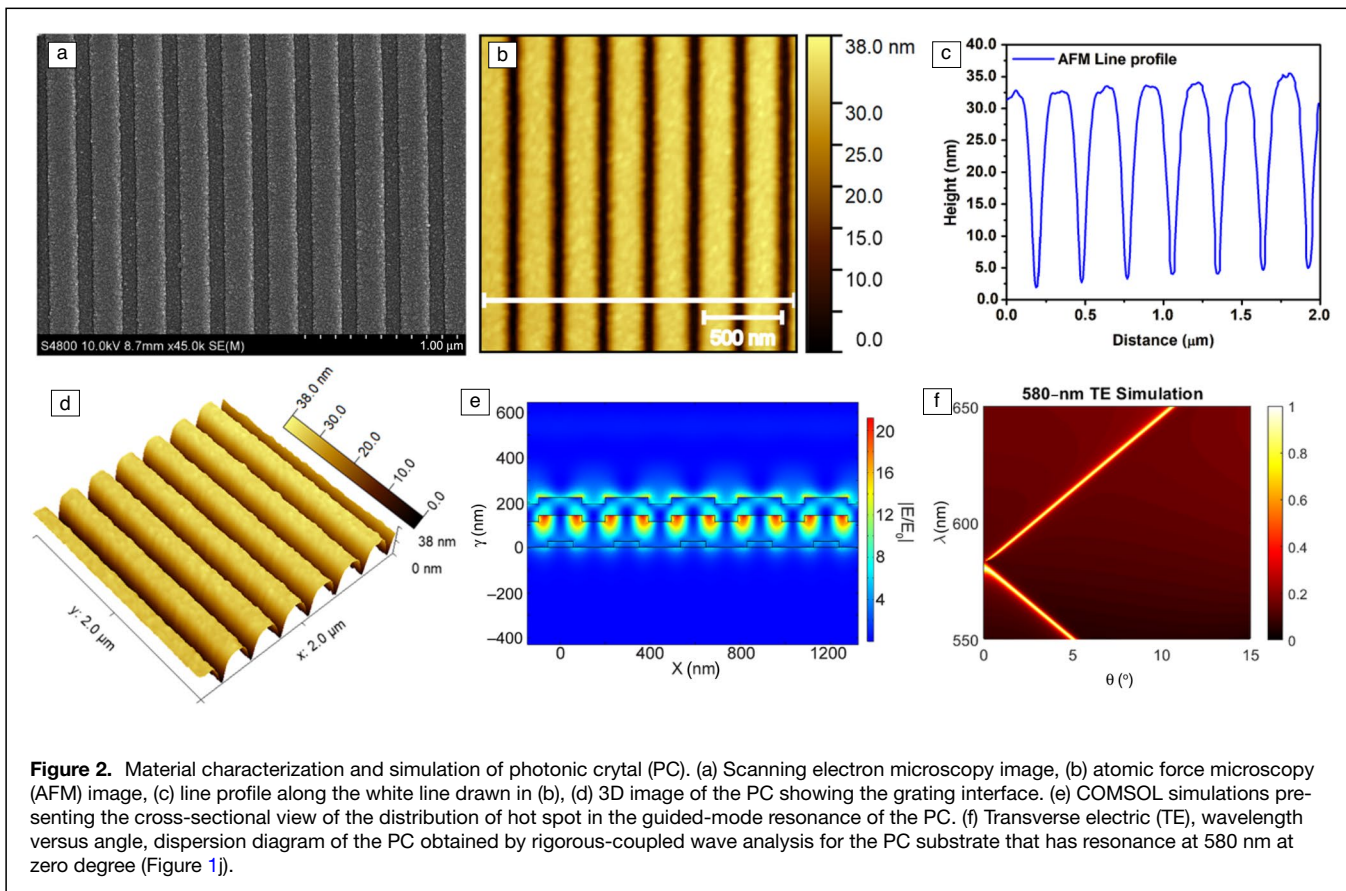
Figure 1. Optical schematic, Au cryosorets (CSs) fabrication, and transmission electron microscopy (TEM) characterization. (a) Optical setup schematic. LWP, long-wave pass; PCES, photonic-crystal-coupled-enhanced steering. (b) Fabrication of AuCS by subjecting the Au nanoparticles (NPs) to adiabatic cooling in LN₂ showing the main steps, including thermal gradient exposure, and thawing to collect the CSs. RT, room temperature. (c) TEM image of AuNP, (d–h) TEM images of the AuCSs obtained by subjecting the AuNPs to different time intervals of LN₂ exposure, namely 15, 30 s, 1, 2, and 3 min, respectively. (i) Conceptual schematic of the photonic crystal (PC) interface with the parameters being $\Lambda=290$ nm, $S_1=110$ nm, $S_2=S_3=S_4=190$ nm; $t_1=t_2=t_3=t_4=28$ nm, $d_1=110$ nm, $d_2=80$ nm, $d_3=60$ nm. The simulated transmittance dips for PC interfaces with and without TiO₂ and PVA for (j) transverse electric (TE) mode and (k) transverse magnetic (TM) mode.

that of the GMR of the PC.⁴⁸ It was noted that the fluorescence enhancements obtained in such a scenario were better than the case where the GMR of the PC was tuned to the excitation maximum of the radiating dipole although the laser wavelength matched the GMR. It was, hence, concluded that in the transmittance mode, a steering fluorescence output can be accomplished by simply placing the sample in between the laser line and the detector, which dramatically reduces the cost of the biosensing platforms.^{48,60,61}

Further, the well-established cryosoret nanoengineering (CSNE)^{44,62} method was utilized to obtain AuCS nanoassemblies using the adiabatic cooling protocol shown in Figure 1b. Under the thermal gradient, the cooling effect outperforms the electrostatic repulsion effect (that exists between the citrate capped negatively charged AuNPs) thereby resulting in the formation of AuCSs with an increasing number of NPs per assembly with the increase in the cooling time interval (Figure 1c–h). A schematic of the PC under study is presented in Figure 1i along with the details of the structural

parameters [$\Lambda=290$ nm, $S_1=110$ nm, $S_2=S_3=S_4=190$ nm; $t_1=t_2=t_3=t_4=28$ nm, $d_1=110$ nm, $d_2=80$ nm, $d_3=60$ nm]. The transmittance dips observed in the wavelength region of interest (475–700 nm) for TE and TM modes obtained via simulations are shown in Figure 1j–k. The TiO₂ coating and subsequent PVA coating over the underlying PC shift the resonance to the higher wavelength, and this is performed so as to bring the resonance of the PC to that of the emission wavelength of the radiating dipole. Extensive characterization of the PC using focused ion beam (FIB)-SEM and AFM for only PC, PC+TiO₂ coating, as well as PC+TiO₂+PVA coating are presented in our recent work.⁴⁸

Fundamentally, there are two methods that are generally utilized to enhance the performance of the fluorescence-based biosensing frameworks: (1) with the use of advanced optical elements such as focusing mirrors and lenses for directing the omnidirectionally emitted photons toward the collection optic fiber/associated detector; and^{63,64} (2) engineering the interface with appropriate nano-patterns and nanoscale



materials in order to furnish high-field enhancement which, in turn, would result in high excitation and emission rates of the fluorophores.^{26,65,66} Lakowicz and co-workers demonstrated such effects by interfacing the radiating dipoles over the surface plasmon polaritons (SPPs) of metal thin film as well as spacer nanoengineering so as to realize high radiative decay rate, high photostability, and augmented fluorescence output.^{11,58,67} This second approach is highly recommended on account of its cost-effectiveness and feasibility to modulate the near-field light–matter interactions at the interface between the radiating dipole and the surface. Although the metal thin-film-based substrates suffer from intrinsic parasitic ohmic losses, our approach is to utilize one-dimensional grating PCs with less lossy attributes and concomitant better performance.^{68–70}

The PC surface structures were extensively characterized using SEM and AFM, and the results are presented in **Figure 2a–b**. The all-dielectric PC substrates were sputter-coated (Au–Pd Sputter Coater) with a 5-nm-thick Au–Pd to yield a conducting surface for better resolution in SEM imaging. The height profile of the grating (depth of the grooves to be ~27 nm) along the line drawn in **Figure 2b** is shown in **Figure 2c**, along with the 3D view of the PC shown in **Figure 2d**. The COMSOL simulations presenting the cross-sectional view of the distribution of the hot spot with enhancement in the high refractive index region (Si_3N_4) of the GMR (of the

PC) is shown in **Figure 2e**. Further, in our previous work,⁴⁸ different thickness of the TiO_2 sputtering was experimentally carried out to arrive at optimized conditions to realize highest fluorescence enhancements. While the bare PC without any TiO_2 coating yielded resonance at ~500 nm, sputtering the substrate with 28 and 80 nm TiO_2 shifted the resonance to ~530 nm (closer to laser excitation), and ~580 nm (closer to dye's emission). As the PC substrate ~580 nm resonance (with 80-nm TiO_2 coating) yielded the highest fluorescence enhancements experimentally for TE polarization of light, in this work, we have used this particular interface for further investigation. This PC was used as the substrate to plot the numerically simulated (or calculated using RCWA, and plotted using MATLAB) dispersion diagram shown in **Figure 2f** with the color bar representing the normalized reflectance in arbitrary units for all simulated dispersion diagrams. As this particular PC substrate presented high-fluorescence enhancements experimentally for the TE-polarized GMR, we have chosen to focus on the TE-coupled fluorescence emission enhancements (the TM-polarized resonances of the PC do not yield high experimental fluorescence intensity as the modes occur with wavelengths less than 550 nm, while we used a 550-nm long-wave pass filter to avoid the laser excitation).

The overall effect of micro-nanofabrication in photonic systems is extensively discussed from the perspective of



macroscopic, mesoscopic, and microscopic levels with SERS or related technologies.^{29,71–74} However, such an elucidation in the case of PCEF is seldom presented, although such an analysis is important to comprehend the light–matter interactions from various perspectives. Here, we make an attempt to highlight the experimental and simulation results of our work from this standpoint. Typically, in the macroscopic level, the light–matter interactions are modulated using the advanced optical elements (such as lenses, mirrors, high-numerical apertures, etc.) even before the light source interacts with the sample and the output spectra is efficiently collected using the same or additional collection tools (advanced microzone Raman spectroscopy is an example where extensive macroscopic engineering is incorporated).^{71,75} Although such macroscopic engineering yields high signal intensity, it is conventionally difficult to decouple the effect of such macroscopic elements from the actual effect of EM-field enhancement. In this regard, in our recent technology, we demonstrated an objective-free, prism-free, and metal thin-film-free PCES emission platform that eliminates the contribution from the macroscopic level (optical scheme shown in Figure 1a).⁴⁸ Here, we showcase the performance of AuCSs vis-à-vis AuNPs in the PCES emission platform where we expect minimal contribution from macroscopic engineering toward the fluorescence enhancements.

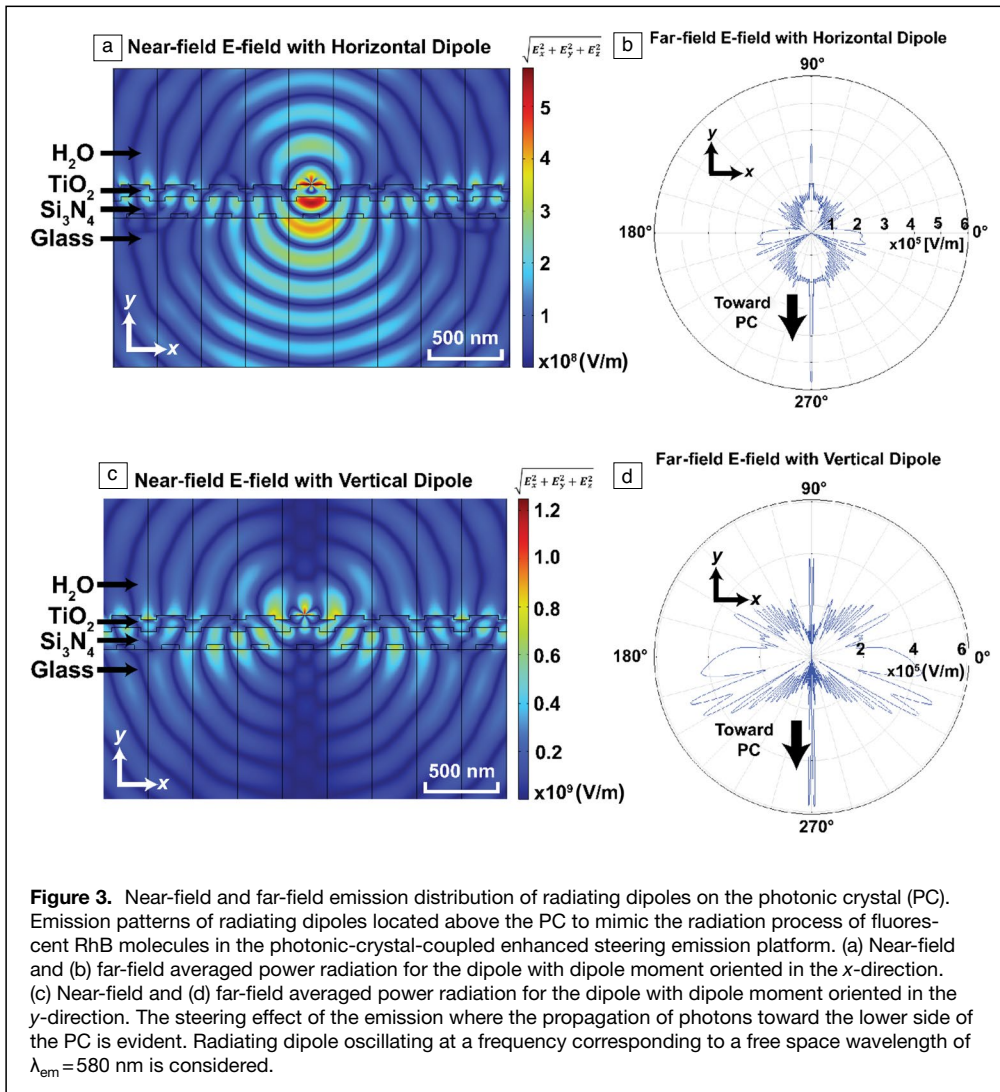
Further, it is informative to discuss the contribution of AuCSs toward PCES emission from mesoscopic and microscopic regimes. At this juncture, it is worth defining the terminologies in order to facilitate the understanding of key highlights of the work. The fluorescence enhancement emerging because of the mesoscopic engineering involves the strategies developed to realize optimal geometric and physical properties of the plasmonic nanosystems under consideration.^{29,71} Whereas the geometric configuration includes the aspects related to shape, size, assembly (dimer, trimer, etc.), and topography to name a few, the physical contribution includes the aspects associated with the substrate design, loss, and gain mechanisms.^{72–74} Further, the microscopic engineering to augment the fluorescence output includes modulating the microscopic light–molecule interactions that are directly associated with the fluorescence coupling efficiency (laser emission–molecular absorption–fluorescence emission) at a particular wavelength and local EM-field enhancement supported by the overall system at identical wavelength.^{29,71,76} Hence, this strategy operates by influencing the electronic, rotational, and vibrational modes of the fluorescent molecules by engineering the local environment.^{24,71} Although these are the general descriptions of the mesoscopic and microscopic strategies, in the subsequent sections, we discuss the careful incorporation of such approaches in our work to realize quenched and augmented fluorescence output.

From a microscopic standpoint, our system is optimized to present large intrinsic fluorescence output as the absorption maximum of the RhB overlaps well with the laser line under consideration. Moreover, the fluorescence outcoupling

is augmented by carefully matching the GMR of the underlying PC with the emission maximum of the radiating dipoles, thereby rendering a large fluorescence cross section. Further, from a mesoscopic engineering perspective, our approach incorporates the use of cryosoret nanoassemblies that present high local electric-field enhancement via three-dimensionally distributed nanovoids and nanorecives.^{44,62} This plasmonic system presents newer decay pathways for the proximal radiating dipoles which experience high radiative decay with concomitant reduced lifetime.^{48,61} Moreover, in accordance with the principles of an induced plasmon effect of metal-enhanced fluorescence (MEF),¹¹ the cryosorets not only enhance the emission from radiating dipoles, but also the radiating dipoles trigger generation of plasmons due to augmented emission, both working in a cascading effect to function as a hybrid radiating species (radiating plasmon model).^{26,77} Overall, it is worth mentioning that our approach of engineering laser excitation to match molecular absorption, GMR tuning to match the molecular emission, and cryosoret incorporation to yield high-field enhancement presents a judicious hybrid coupling approach where the microscopic and mesoscopic strategies collectively operate. In order to obtain theoretical insights about such speculations, the near-field and far-field emission patterns of the radiating dipole placed over a PC are investigated and the results are captured in Figure 3.

Fundamentally, a grating-based PC performs the following dual role: (a) the grating localizes the GMR into specific hot spot domains where the molecules experience high-field intensity thereby supporting surface-enhanced spectroscopy,^{45,46,78,79} (b) the light that is coupled to the GMR of the grating PC is channelized into the specific allowed modes detailed in the dispersion diagram of the PC.^{46,80,81} Consequently, the light diffraction and scattering attribute of the grating directs the emitted photons from a proximal fluorophore into certain modes. Further, a fluorescent molecule may be visualized as an entity that transforms energy from higher frequency (lower wavelength) to lower frequency (higher) during the fluorescence emission process, under appropriate excitation.^{5,82} Typically, the radiating dipole has minimal influence on the EM-field intensity of surrounding medium during the excitation and emission process. Although this is true for ideal situations (case where the radiating dipole is in vacuum or homogenous medium), in practical scenarios involving mesoscopic and microscopic engineering, the above hypothesis is invalid, thereby demanding simulation tools to validate the understanding (or speculate experimental results).^{71,72}

In this background, we have performed the COMSOL simulations for radiating dipole (oscillating at a frequency corresponding to a free space wavelength of $\lambda_{em} = 580$ nm) placed over the PC in order to mimic the radiation process of fluorescent RhB molecules in the PCES emission platform. The near-field radiation pattern and far-field averaged power radiation for the dipole oriented in the x -direction are shown in Figure 3a–b (for electric-field component), in accordance with earlier works.^{83–86} The same for the dipole oriented in the y -direction



are shown in Figure 3c–d. From the near-field pattern, for the dipole oriented in the x-direction, it is clear that the emission is enhanced toward the PC side *vis-à-vis* the FS side. More importantly, it is observed that the near-field pattern presents the movement of photons right below the PC surface after coupling with the PC (also substantiated by far-field distribution shown in Figure 3b). In addition to this from Figure 3b, d, we see that the far-field emission pattern is directed right below the PC irrespective of the radiating dipole orientation.⁸³ Such observations made in the simulation validates the hypothesis of the radiating GMR model presented via experimental observations in our recent work.⁴⁸ In other words, the near-field emission pattern depicting a steering photon output resembles the experimentally obtained steering emission output (in addition to the emergence of the modes at zero degrees, Figure 2f). These computer-assisted simulation results validate the following aspects: (1) the emission from the radiating dipole is sufficient to trigger/generate GMR and a direct laser excitation of the GMR is not necessary; (2) the emitted photons from radiating dipoles further are coupled with the GMR, highly localized in the near

field, and yield boosted fluorescence output toward the PC-coupled side (as compared to free space side) toward the far field; and (3) the “radiating dipole-PC” conjugate, hence, functions as a hybrid entity that radiates the PC-coupled emission to the far field with highly desirable steering fluorescence output. Further, the simulations performed using different representative nanoassemblies (dimer, trimer, and so on) reemphasize the fact that the emission pattern in the far field shows a steering fluorescence output, irrespective of the number of NPs per assembly (Supplementary information Figures S1–S5). Further, a representative example of tetramer is considered to understand the far-field emission pattern by changing its location on the grating PC with results captured in Figure S6. It is observed that, regardless of the precise location of the nanoassembly on the grating photonic crystal (PC), the far-field emission from the radiating dipole is predominantly directed straight beneath the PC. This result corroborates the experimental observations. It is important to mention that the simulations with a large number of periods, extremely small mesh sizes, or additional smoothing could yield more refined plots at the cost of substantially greater computing resources. Our focus in this section is to demonstrate the general emission patterns of the radiating dipole under consideration and their alignment with experimental results. Given that the current data effectively capture the main findings of the study, the presented simulated data sufficiently support the experimental observations. The analysis of simulations presented above forms a solid basis for understanding and planning the experimental work, where we envisage such microscopic and mesoscopic effects to coexist and function productively yielding intriguing experimental PC-coupled fluorescence.

By and large, the limitations of conventional fluorescence spectroscopy-based detection systems include isotropic

emission, lesser photostability of luminescent species, trivial cross sections that ultimately make the quantification of the analytes at extremely low concentrations very difficult.^{61,70} In spite of the fact that the fluorescence emission is an inherent property of the radiating dipole, in practical scenarios, the emission is substantially modulated (increased or quenched) in the presence of a proximal interface that is close to the emitting species. The cumulative radiative decay output is determined by the photonic mode density (PMD) rendered by this interface as well as the countering nonradiative pathways (that result in quenching). The local density of states rendered by the adjacent interfaces (made of plasmonic or dielectric substrates) have been used to modify the overall emission output. In our experiments, as the AuNPs absorb predominantly in the emitting region of the EM spectrum (of the radiating dipoles used), the quenching observed is substantial. In this background, the major two approaches that have been employed in maximizing the overall fluorescence

output are (1) augmenting the EM-field intensity in the near field of the radiating dipoles that supply higher PMDs^{21–23,26} and (2) utilizing methods to dwindle the quenching effect (or realize dequenching effect).^{24,87} In this report, the former objective is accomplished by exciting the pair of counterpropagating leaky modes in the corrugated guiding layer of the PC, from which stationary wave patterns are formed generating the evanescent field at the PC-dielectric, thereby yielding steering fluorescence output. Further, the second objective is achieved using the AuCSs that present large optical cross sections, high LDOS, via the hottest plasmonic hot spots. The overall experimental output is shown as a conceptual schematic in **Figure 4a**.

While the PCCE emission platform yielded 24-fold fluorescence enhancements *vis-à-vis* glass interface, the incorporation of AuNPs in the cavity interface presented quenched ~10-fold enhancements. This is attributed to the surface-induced quenching effects

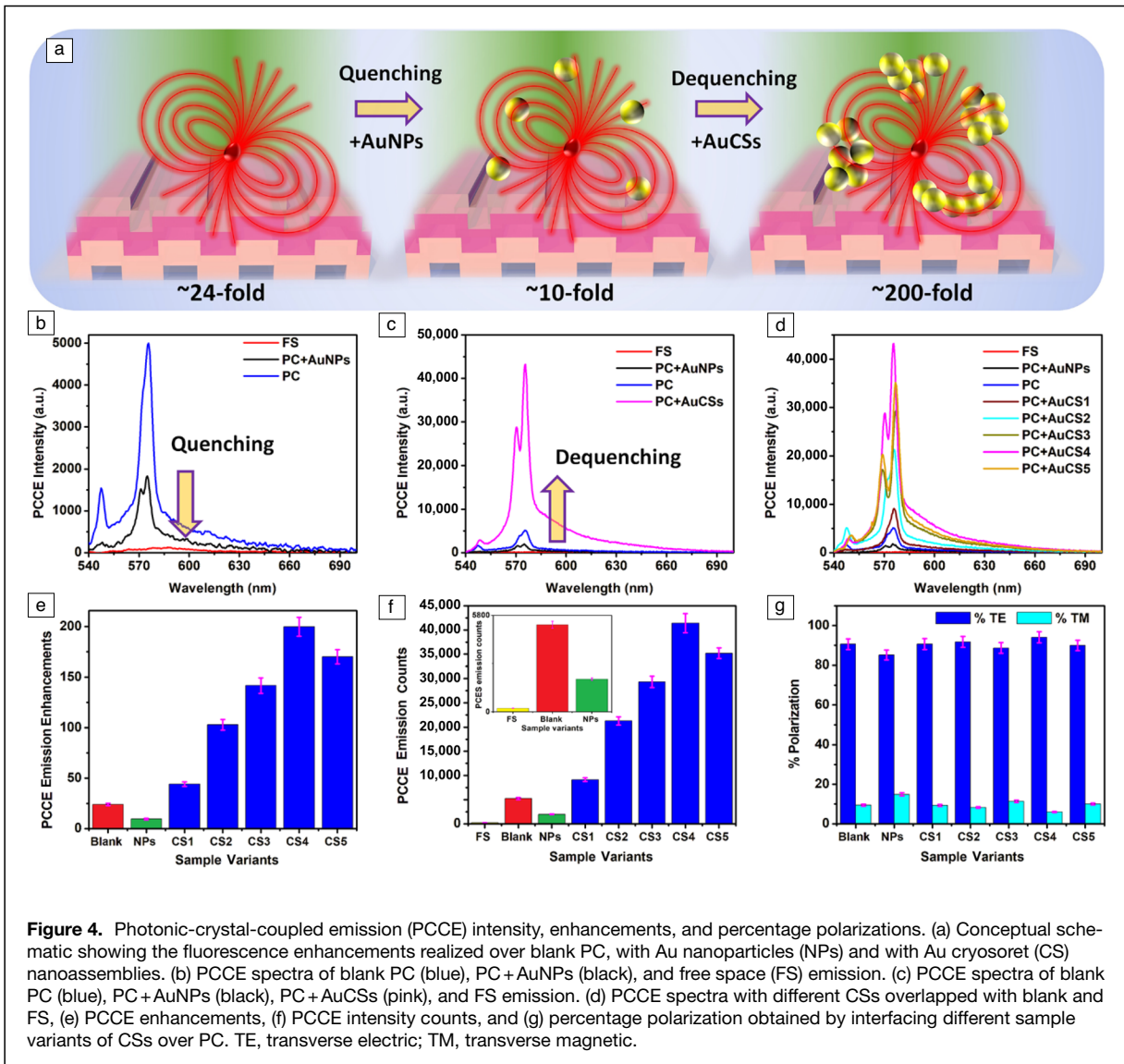


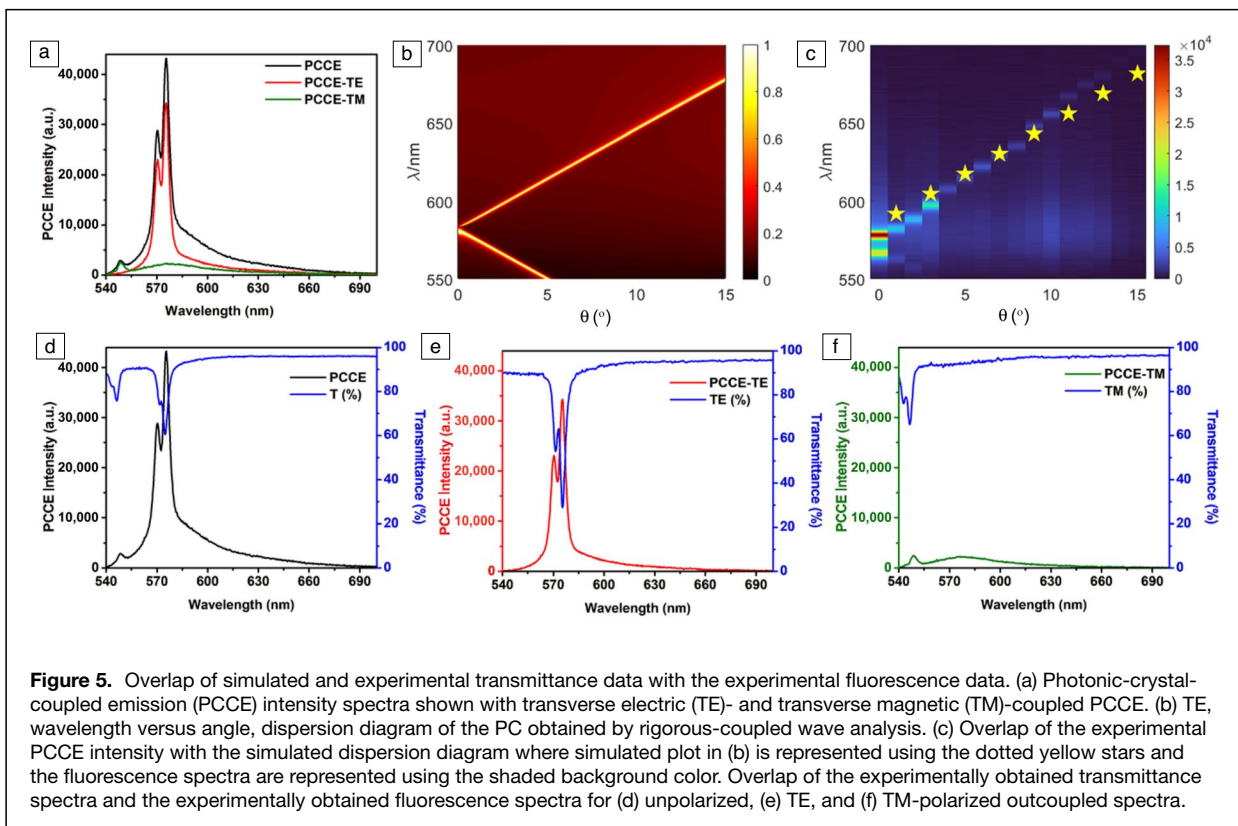
Figure 4. Photonic-crystal-coupled emission (PCCE) intensity, enhancements, and percentage polarizations. (a) Conceptual schematic showing the fluorescence enhancements realized over blank PC, with Au nanoparticles (NPs) and with Au cryosoret (CS) nanoassemblies. (b) PCCE spectra of blank PC (blue), PC + AuNPs (black), and free space (FS) emission. (c) PCCE spectra of blank PC (blue), PC + AuNPs (black), PC + AuCSs (pink), and FS emission. (d) PCCE spectra with different CSs overlapped with blank and FS. (e) PCCE enhancements, (f) PCCE intensity counts, and (g) percentage polarization obtained by interfacing different sample variants of CSs over PC. TE, transverse electric; TM, transverse magnetic.



(interband transitions) rendered by the plasmonic AuNPs, while they are admixed with the radiating dipoles. However, the same substrate fabrication steps followed using the Au cyosorets yielded dequenched ~ 200 -fold PCCE enhancements because of the high-field enhancement supported by the nanoassemblies.^{19,44,45} Moreover, while the nanovoids and nanorecives in and around the AuCSs facilitate the optical field entrapment and generation of void plasmons, interfacing them over the PC interface (that sustains GMR) results in the generation of cavity-driven hot spots. The quenching and dequenching in the PCCE spectra recorded by interfacing the AuNPs and AuCSs over the PC are shown in Figure 4b–c. The PCCE spectra obtained for all the samples (AuCS1–5) under consideration are shown in Figure 4d, where we clearly see a gradual increase in the PCCE intensity counts for samples from AuCS1 to AuCS4, and a subsequent decline for AuCS5 variant. The PCCE emission enhancements calculated as the ration of the PCCE intensity counts (Figure 4f) and free space (FS) intensity counts are shown in Figure 4e along with the data of the percentage polarization shown in Figure 4g for triplicate measurements. The percentage polarization is calculated using the formula: % TE = [TE counts \div (TE + TM counts)] * 100, where counts represent the fluorescence intensity counts obtained using that particular polarizer between the PC substrate and the detector. The consistently high TE percentage polarization output of the steered emission validates the generation of PC-coupled emission, and the robust performance of the device.

Further, it is important to discuss the mechanism that results in the high experimental fluorescence output for the use of AuCSs and the peculiarity in the trend of fluorescence. The factors that influence the boosted fluorescence output may be listed as follows: (a) The PCCE emission phenomenon supported by the underlying PC assists by providing newer high radiative decay channels. This is verified with a reduction in the fluorescence lifetime and high photostability, as reported earlier.^{48,57} (b) Hybrid coupling of the delocalized Bragg plasmons sustained by the nanovoids and nanorecives with that of the GMR of the PC interface.^{26,56} (c) Hybrid coupling of the localized plasmons (sustained by the entire AuCS) with that of the GMR of the PC interface.^{11,26,45} Further, as the number of NPs per assembly increases, the three-dimensionally distributed hot spots in the AuCSs increase thereby generating an increasing trend in the fluorescence intensity.^{88–90} However, it is to be noted that excess growth of the nanoassembly would result in counterproductive effects where the superfluous number of NPs per assembly dominates the surface-induced quenching effects.⁴⁴ Hence, the AuCS4 yields the optimum number of inter- (between the PC and AuCS) and intra- (between the AuNPs per assembly) plasmonic hot spots with the most productive and effective number of NPs per assembly, thereby generating the highest fluorescence enhancements.

For the sample variant that yielded highest fluorescence enhancements (~ 200 -fold), the fluorescence spectral overlap with the simulated and experimental transmittance data is captured in Figure 5. The high polarization selectivity of the PC is





clearly demonstrated with the incorporation of the polarizer. The TM-polarized and TE-polarized outcoupled emission is shown in Figure 5a along with the unpolarized emission spectra. While the computer-simulated dispersion diagram is shown in Figure 5b, the overlap of the same with the experimental fluorescence data is shown in Figure 5c. To ease the visual understanding, we have presented both purely simulated dispersion diagram (Figure 5b) and overlap (Figure 5c) of the simulated dispersion diagram (shown as yellow-dotted stars) with the experimental fluorescence data (shaded region) side by side. Clearly, an excellent overlap between the two is observed thereby showcasing the robustness of the AuCS-PC interface for dequenching the fluorescence signal intensity in a wide range of angles (as the dispersion diagram is angle versus wavelength). Further, the overlap of the experimentally recorded fluorescence spectra with the experimentally obtained transmittance measurements for unpolarized, TE-polarized, and TM-polarized data is presented in Figure 5d–f, respectively. While the unpolarized output fluorescence couples with both the TE and TM modes supported by the underlying PC, the incorporation of a polarizer presents selective coupling to the respective modes, thereby cross-validating the earlier understanding of the radiating GMR model.

The actual transmission of emitted light is governed by the phase-matching conditions at the metal–dielectric interface in a typical surface plasmon resonance (SPR) platform.⁶¹ It is ideal to obtain actual transmission normal to the surface of the platform, where the detector can be placed in the same axis as that of the laser source, which would significantly reduce the cost of the detection system while performing fluorescence experiments.^{48,60} However, with the metal–dielectric platforms, it is not feasible to extract emission in the direction of the laser source, because of the dispersive nature of the prism.^{60,63} In this context, different technologies such as metal–dielectric–metal (MDM)^{60,91,92} and Tamm state-coupled emission (TSCE)^{55,93} have been explored to obtain a direct transmission of the emission onto the detector. Such technologies have the advantage of having a laser source and the detector fixed at a particular position rather than moving them (using a 360° rotating stage) to collect the directional emission. However, such methodologies come across with the tradeoff with respect to high cost and multistep substrate fabrication limitations. Another approach that may be adopted for obtaining the emission perpendicular to the sample surface without moving the detector is by collecting all the directional emission into a single point with the use of different lenses and mirrors.⁶³ In this regard, we have used the photonic crystal framework and performed the nanoengineering using cryosorets so as to enhance the sensitivity of the device by minimizing the cost involved, catering to resource-limited settings. While the PC assists in presenting high-field intensity because of the guided mode resonance,¹ the cryosoret nanoassemblies assist in plasmon-enhanced fluorescence on the PC interface.⁴⁴ We have avoided the use of MDM and TSCE as well

as additional lenses and instead used effective nanoengineering methods, so as to develop the technology feasible for low-and-middle-income countries.

Further, it is informative to comment on the importance of utilizing cryosoret nanoassemblies *vis-à-vis* other nanoassembly approaches. Broadly, there are numerous methodologies for achieving the self-assemblies of nanostructures such as (1) template-based (hard and soft templates); (2) hierarchical; (3) directed; and (4) co-assembly; (5) chemical stimuli-based (solvent, acid/base, ions, macromolecules, gases, and redox reactions); (6) physical stimuli-based (such as electric field, magnetic field, light triggered, and temperature driven).^{40,41,44} Among them, the physical stimuli-based self-assembled nano-materials stand out as they largely preserve the physicochemical characteristics of the initial starting nanoscale materials used in the formation of the self-assembly. On the other hand, other types of self-assembled structures often have an/a few additional material/s that sustains the fabric of the self-assembled structure, thereby being template dependent (for instance, DNA structures can be used to generate nanoassemblies where DNA strands enforce the nanogap separation between the NPs in the assembly). The cryosoret nanoassemblies present intriguing substrate for realization of abundant three-dimensionally distributed plasmonic hot spots without the use of any external chemical agent to preserve the self-assembled structure by virtue of the synthesis process.⁴⁴ The adiabatic cooling method developed brings in high chemical and structural stability as detailed in our earlier works via a template-free fabrication approach.^{19,44,45} This is of significant relevance for the current work as the cryosorets enable the elimination of chemical enhancement mechanisms of the fluorescence signal from radiating dipoles (as the emitters situated in close proximity to NPs of the cryosorets are largely quenched) and support only the EM-field enhancement. Therefore, the effect of nanovoids (between the NPs in the self-assembly) and nanocavities (between cryosoret and PC), independently contributes to the overall fluorescence enhancements, in spite of the unavoidable surface-induced quenching. Hence, our approach using AuCSs presents a practical, reliable, and reproducible methodology to overcome the tradeoff between the requirement for augmented emission enhancements and quench-free AuNP-based substrates, and presents itself as a promising platform to the future developments in PCEF technology.

Further, it is informative to discuss the wide-ranging applications of this work from the perspective of possibilities for metamaterial design and associated application. While the magnetic permeability defines the magnetic response of a material, it is typically weak especially in the visible region of the electromagnetic (EM) spectrum.^{93–95} This is because the magnetic counterpart of the EM spectrum interacts weakly (four orders of magnitude less) with conventional materials.⁹³ The initial studies of generating metamaterials with magnetic effects were reported using split-ring resonators, which are basically plasmonic structures that engender artificial magnetism because of the magnetic plasmons and the excitation



of displacement currents.⁹⁶ Although such resonances are difficult to excite in the optical regime due to increased radiation losses, a new classification of materials with effective excitation of resonant displacement currents have emerged with the use of nanoassemblies.⁹³ Plasmonic nanoassemblies are capable of generating artificial magnetism in visible wavelengths where one can modulate the spectral positions and profiles with low losses. Controlled assembly of nanomaterials has been used for infrared magnetic field enhancement,⁹⁷ metamaterial generation,^{98,99} subwavelength plasmonic metamolecule,¹⁰⁰ and strong magnetic field nanofocusing¹⁰¹ to name a few. In a recent study, a family of plasmonic analogs of aromatic molecules (benzene-like building block), presenting magnetic plasmons directly resembling the delocalized orbitals of aromatic hydrocarbon molecules are investigated.¹⁰² Because the cryosoret nanoassembly enables the generation of nanoassemblies with high control over the number of nanomaterials per assembly, we anticipate their utility in the exploration of metamaterial substrate fabrication and associated applications. It must not go without mention that although we can tune the number of nanomaterials per assembly in the cryosorets, the major limitation of structural anisotropy still remains a major challenge from the perspective of precision nanoengineering. While the advanced nanoengineering methods, for instance, using DNA origami yields nanoassemblies with precise nanogaps between every single structural unit with high isotropic, this control over the distribution of nanomaterials in the cryosorets has not been achieved yet, by virtue of the synthesis method. However, ensemble spectroscopic or imaging measurements where the structural anisotropy negligibly impacts the overall results can still benefit from the cryosoret nanoassemblies especially because of the ease of synthesis method and low cost.

Radiating GMR model

It is instructive to discuss the concepts and mechanism of the radiating GMR resonance model from the perspective of the radiating plasmon model and radiating surface wave model. Researchers are progressively looking at plasmonic/metallic nanoparticles (NPs) with unique optical functions to enhance the effectiveness of traditional fluorescence-based detection methods. In the near proximity of a plasmonic nanostructure, there is a considerable change in the fluorescence excitation and emission of a radiating dipole.^{11,61} The fluorescence intensity changes dramatically as a result of the high electric-field intensity (caused by a high effective extinction coefficient) that plasmonic NPs create in the near field. Furthermore, the oscillating charge densities on metal NPs interact with the excited fluorophores to produce plasmons, which ultimately radiate into detectable far-field radiation. This concept is well established as an induced plasmon effect of MEF,¹⁰³ where the radiating dipoles induce the generation of plasmons that eventually couple into a hybrid emitting species.^{10,55,61} These characteristics of plasmon-fluorophore interactions are well elucidated by Lakowicz and co-workers

in a series of publications termed “radiative decay engineering 1–8” where a powerful technology termed surface plasmon-coupled emission (SPCE) is described experimentally and theoretically.^{61,64,93,103–107} The SPCE research may be conducted using one of two experimental configurations: (1) Kretschmann Raether (KR) or (2) Reverse Kretschmann (RK).^{108,109} In the RK configuration, the fluorophores are directly excited by the laser light at normal incidence to the substrate. Surface plasmon polaritons (SPPs) are produced when these excited fluorophores couple with the Ag thin film’s surface plasmons. According to the radiating plasmon model, even if the fluorophores are excited by the laser illumination directly in RK configuration, those that are within a fractional wavelength of the underlying metal film couple with the surface plasmons to produce SPCE (as the excitation is equal across the thickness of the sample). The far-field outcoupled emission is then gathered from the prism’s distal portion using an optical fiber. As a result, unlike in the KR arrangement, the laser does not directly excite the surface plasmons to produce evanescent fields. The hybrid system of the fluorophore over the metal thin film is referred to as the plasmophore (or plasmon-coupled fluorophore) because the far-field emission in the SPCE platform includes the characteristics of the fluorophore (in terms of spectra) and the characteristics of the plasmonic resonance of the metal–dielectric interface (in terms of TM-polarized resonance coupling).^{65,110,111} Hence, the plasmophores (plasmon-coupled luminophores) function as a single emitting/radiating species justifying the title “radiating plasmon model.”^{10,11,103}

With this as motivation, the mechanism of a radiating GMR model may be summarized as follows: first, the laser illuminates the radiating dipoles that are interfaced with the underlying PC (it must be noted that the laser is not directly exciting the resonance of the PC). Second, as the emission maximum of the radiating dipoles overlap with the GMR of the PC, the emitted photons from the radiating dipoles effectively excite the GMR. Third, the excited GMR now generates high-field enhancement at the interface because the fluorescence is enhanced (enhanced emission).⁴⁸ From our experiments, we noted that the far-field emission observed at the detector is seen to have the characteristic spectral signature of the radiating dipole as well as the polarization selectivity rendered by the underlying PC. Hence, the outcoupled emission can be visualized as a PC-coupled emission from a single hybrid emitting entity (which is a combination of PC and radiating dipole).⁴⁸ Further, interfacing plasmonic cryosorets in such configurations results in very interesting phenomena on account of their localized Mie and delocalized Bragg plasmons,^{44,45,62} and the sequence of events may be listed as follows: (1) laser excites the radiating dipoles and the latter emits photons; (2) the emitted photons from radiating dipoles excite the LSPR of the adjacently located nanomaterials (in this case, the cryosorets); (3) simultaneously (with [2]), the radiating dipoles excite the GMR of the underlying PC; (4) the excited GMR of the PC sustains regions of high-field



intensity termed “hot spots” that further enhance the fluorescence emission; and (5) synergistic hybridization of plasmonic nanogap-induced hot spots from cryosorets and hot spots from GMR yields very high local density of states for the proximal radiating dipoles, which is experimentally observed as high-fluorescence enhancements.

Conclusions

Quenching effects observed in the combination of plasmonic nanomaterials and the fluorescent moieties have remained a long-standing challenge in the broad domain of nanoplasmonics and related biosensing modalities. Fundamentally, the quenching phenomenon emerges because of the undesirable plasmonic modes, nonradiative channels including but not limited to inter- and intra-band transitions, electron scattering, electron–hole pair generation, and ohmic losses. Although more efficient fluorescence signal intensities may be achieved using appropriate substrate design and incorporation of active spacer material, the suppression in the quenching realized is subject to experimental artifacts. Incorporation of nanoassemblies with effective nanovoids increases the photonic mode density with large cross sections for efficient excitation and emission of proximal fluorophores. In this work, the Au cryosoret nanoassemblies are fabricated and interfaced with the PC to realize not only dequenched, but also amplified fluorescence output because of the dual effect of hybrid coupling between the GMR of the PC and the plasmons of cryosoret nanoassemblies. The computer-simulated dispersion diagrams are substantiated with the experimentally obtained tunable and polarized fluorescence data with an excellent overlap between them. Moreover, the insights from COMSOL Multiphysics simulations corroborate our theoretical predictions of the radiating GMR model, presenting a new window to further explore the usefulness of the model with other hybrid polaritonic systems such as low-dimensional substrates (such as graphene analogous), quantum dots, and nanodiamonds. We believe that the synergistic approach of hybridizing Au cryosorets with PC developed in this work for realizing dequenched fluorescence enhancements is of immediate relevance to the broad audience of nanophotonics and biosensing, for applications relating to point-of-care diagnostics and chem-biosensing.

Acknowledgments

S.B. thanks the research scientists E. Araud, K. Walsh, Y. He, W. Swiech, D. Nall, U. Doha, and G. Fried for their support and research inputs in characterization of materials. The support from the IGB Core Facilities, instruments including Cypher AFM Asylum, Research WITec Alpha 300 RA Raman-AFM-SNOM, and Confocal-Zeiss LSM 710-Multiphoton Microscope, as well as the Clean room facility and BioNanotechnology Laboratory (BNL) at Nick Holonyak Jr. Micro and Nanotechnology Laboratory (HMNTL) and the associated research scientists are gratefully acknowledged. The support from the instruments Asylum Research MFP-3D

AFM; Hitachi S-4800 High Resolution SEM; Au-Pd Sputter Coater—Emscope SC 500; and JEOL 2100 CRYO TEM, the associated staff and research scientists at Materials Research Laboratory, The Grainger College of Engineering, the University of Illinois at Urbana-Champaign is gratefully acknowledged. The authors thank the feedback provided by all the members of the Nanosensors group, HMNTL, during scientific discussions.

Author contributions

Conceptualization: S.B., L.L.; Methodology: S.B., L.L., W.L.; Formal analysis and investigation: S.B., L.L., W.L., and J.T.; Writing—original draft preparation: S.B., L.L., W.L., and J.T. Writing—review and editing: S.B., L.L., B.T.C.; Funding acquisition: S.B., B.T.C.; Resources: B.T.C.; Supervision: B.T.C.

Funding

The authors gratefully acknowledge funding from the National Institutes of Health (Nos. R01AI159454, R01CA227699, R01AI139401, R01EB029805, and RadXRad Program Grant No. U01AA029348) and the National Science Foundation (NSF RAPID 20-27778, CBET 19-00277, and CBET 22-32681). Financial support was also provided by the Cancer Center at Illinois. J.T. is supported by the Illinois Distinguished Fellowship and the National Science Foundation Graduate Research Fellowship. S.B. is supported by a postdoctoral fellowship from the Carl R. Woese Institute for Genomic Biology.

Data availability

The data that support the findings of this study are available from the corresponding authors upon reasonable request.

Conflict of interest

The authors have no conflicts to disclose.

Supplementary Information

The online version contains supplementary material available at <https://doi.org/10.1557/s43577-024-00850-2>.

References

1. N. Ganesh, W. Zhang, P.C. Mathias, E. Chow, J.A.N.T. Soares, V. Malyarchuk, A.D. Smith, B.T. Cunningham, *Nat. Nanotechnol.* **2**(8), 515 (2007). <https://doi.org/10.1038/nnano.2007.216>
2. L. Syedmoradi, M. Daneshpour, M. Alvandipour, F.A. Gomez, H. Hajghasem, K. Omidfar, *Biosens. Bioelectron.* **87**, 373 (2017). <https://doi.org/10.1016/j.bios.2016.08.084>
3. R.M. Bakker, H.-K. Yuan, Z. Liu, V.P. Drachev, A.V. Kildishev, V.M. Shalaev, R.H. Pedersen, S. Gresillon, A. Boltasseva, *Appl. Phys. Lett.* **92**(4), 043101 (2008). <https://doi.org/10.1063/1.2836271>
4. D. Rout, R. Vijaya, *J. Appl. Phys.* **119**(2), 023108 (2016). <https://doi.org/10.1063/1.4939775>
5. J.-F. Li, C.-Y. Li, R.F. Aroca, *Chem. Soc. Rev.* **46**(13), 3962 (2017). <https://doi.org/10.1039/C7CS00169J>
6. S.-Y. Ding, J. Yi, J.-F. Li, B. Ren, D.-Y. Wu, R. Panneerselvam, Z.-Q. Tian, *Nat. Rev. Mater.* **1**(6), 16021 (2016). <https://doi.org/10.1038/natrevmats.2016.21>



7. S. Bhaskar, S.S.M. Lis, S. Kanvah, B.N.S. Bhaktha, S.S. Ramamurthy, *ACS Appl. Opt. Mater.* **1**(1), 159 (2023). <https://doi.org/10.1021/acsaom.2c00026>
8. W.J. Wing, S.M. Sadeghi, R.R. Guttha, Q. Campbell, C. Mao, *J. Appl. Phys.* **118**(12), 124302 (2015). <https://doi.org/10.1063/1.4931378>
9. J. Zhang, L. Zhang, W. Xu, *J. Phys. D Appl. Phys.* **45**(11), 113001 (2012). <https://doi.org/10.1088/0022-3727/45/11/113001>
10. J.R. Lakowicz, *Plasmonics* **1**(1), 5 (2006). <https://doi.org/10.1007/s11468-005-9002-3>
11. J.R. Lakowicz, K. Ray, M. Chowdhury, H. Szmazinski, Y. Fu, J. Zhang, K. Nowaczyk, *Analyst* **133**(10), 1308 (2008). <https://doi.org/10.1039/B802918K>
12. P. Mulpur, S. Yadavilli, A.M. Rao, V. Kamiseti, R. Podila, *ACS Sens.* **1**(6), 826 (2016). <https://doi.org/10.1021/acssensors.5b00297>
13. S. Baher, Z. Lorestaniweiss, *J. Appl. Phys.* **124**(7), 073103 (2018). <https://doi.org/10.1063/1.5031191>
14. T.K. Hakala, J.J. Toppari, A. Kuzyk, M. Pettersson, H. Tikkanen, H. Kunttu, P. Törmä, *Phys. Rev. Lett.* **103**(5), 053602 (2009). <https://doi.org/10.1103/PhysRevLett.103.053602>
15. Y. Chen, L. Chen, K. Wen, Y. Hu, W. Lin, *J. Appl. Phys.* **126**(8), 083102 (2019). <https://doi.org/10.1063/1.5105358>
16. M.-C. Daniel, D. Astruc, *Chem. Rev.* **104**(1), 293 (2004). <https://doi.org/10.1021/cr030698+>
17. V. Dobrokhotov, D.N. McIlroy, M.G. Norton, A. Abuzir, W.J. Yeh, I. Stevenson, R. Pouy, J. Bochenek, M. Cartwright, L. Wang, J. Dawson, M. Beaux, C. Berven, *J. Appl. Phys.* **99**(10), 104302 (2006). <https://doi.org/10.1063/1.2195420>
18. K. Saha, S.S. Agasti, C. Kim, X. Li, V.M. Rotello, *Chem. Rev.* **112**(5), 2739 (2012). <https://doi.org/10.1021/cr2001178>
19. V.S.K. Cheerala, K.M. Ganesh, S. Bhaskar, S.S. Ramamurthy, S.C. Neelakantan, *Langmuir* **39**(22), 7939 (2023). <https://doi.org/10.1021/acs.langmuir.3c00801>
20. E. Mukherjee, J. Pillanagrovi, D. Bhatnagar, S. Dutta-Gupta, *J. Appl. Phys.* **133**(7), 073101 (2023). <https://doi.org/10.1063/5.0132791>
21. N. Kongsuwan, A. Demetriadou, R. Chikkaraddy, F. Benz, V.A. Turek, U.F. Keyser, J.J. Baumberg, O. Hess, *ACS Photonics* **5**(1), 186 (2018). <https://doi.org/10.1021/acsp Photonics.7b00668>
22. R. Faggiani, J. Yang, P. Lalanne, *ACS Photonics* **2**(12), 1739 (2015). <https://doi.org/10.1021/acsp Photonics.5b00424>
23. J. Yang, R. Faggiani, P. Lalanne, *Nanoscale Horiz.* **1**(1), 11 (2016). <https://doi.org/10.1039/C5NH00059A>
24. S. Bhaskar, N.C.S.S. Kowshik, S.P. Chandran, S.S. Ramamurthy, *Langmuir* **36**(11), 2865 (2020). <https://doi.org/10.1021/acs.langmuir.9b03869>
25. C. Dahmen, B. Schmidt, G. Von Plessen, *Nano Lett.* **7**(2), 318 (2007). <https://doi.org/10.1021/nl062377u>
26. S. Bhaskar, P. Das, M. Moronshing, A. Rai, C. Subramaniam, S.B.N. Bhaktha, S.S. Ramamurthy, *Nanophotonics* **10**(13), 3417 (2021). <https://doi.org/10.1515/nanoph-2021-0124>
27. A. Rai, S. Bhaskar, S.S. Ramamurthy, *ACS Appl. Nano Mater.* **4**(6), 5940 (2021). <https://doi.org/10.1021/acsanm.1c00841>
28. A. Bek, R. Jansen, M. Ringler, S. Mayilo, T.A. Klar, J. Feldmann, *Nano Lett.* **8**(2), 485 (2008). <https://doi.org/10.1021/nl072602n>
29. H. Yu, Y. Peng, Y. Yang, Z.-Y. Li, *NPJ Comput. Mater.* **5**(1), 45 (2019). <https://doi.org/10.1038/s41524-019-0184-1>
30. S. Bhaskar, R. Patra, N.C.S.S. Kowshik, K.M. Ganesh, V. Srinivasan, S.P. Chandran, S.S. Ramamurthy, *Phys. E Low Dimens. Syst. Nanostruct.* **124**, 114276 (2020). <https://doi.org/10.1016/j.physe.2020.114276>
31. M. Blanco-Formoso, N. Pazos-Perez, R.A. Alvarez-Puebla, *Nanoscale* **12**(28), 14948 (2020). <https://doi.org/10.1039/D0NR04167J>
32. A. Kinkhabwala, Z. Yu, S. Fan, Y. Avlasevich, K. Müllen, W.E. Moerner, *Nat. Photonics* **3**(11), 654 (2009). <https://doi.org/10.1038/nphoton.2009.187>
33. K. Kneipp, H. Kneipp, "Surface Enhanced Raman Scattering Using the 'Hottest' Hot Spots Only," in *Proceedings of the Imaging and Applied Optics Congress (2010)* (Optica Publishing Group, Washington, DC, 2010), p. MMB1. https://doi.org/10.1364/PMETA_PLAS.2010.MMB1
34. K. Kneipp, H. Kneipp, "Non-resonant SERS Using the Hottest Hot Spots of Plasmonic Nanoaggregates," in *Frontiers of Surface-Enhanced Raman Scattering: Single Nanoparticles and Single Cells* (Wiley, 2014), chap. 2, pp. 19–35. <https://doi.org/10.1002/9781118703601.ch2>
35. P. Pavaskar, S.B. Cronin, *Appl. Phys. Lett.* **94**(25), 253102 (2009). <https://doi.org/10.1063/1.3157168>
36. K. Kneipp, Y. Wang, H. Kneipp, L.T. Perelman, I. Itzkan, R.R. Dasari, M.S. Feld, *Phys. Rev. Lett.* **78**(9), 1667 (1997). <https://doi.org/10.1103/PhysRevLett.78.1667>
37. K. Li, M.I. Stockman, D.J. Bergman, *Phys. Rev. Lett.* **91**(22), 227402 (2003). <https://doi.org/10.1103/PhysRevLett.91.227402>
38. S. Kadkhodazadeh, J.B. Wagner, V. Joseph, J. Kneipp, H. Kneipp, K. Kneipp, *Plasmonics* (Norwell, Mass.) **8**(2), 763 (2013). <https://doi.org/10.1007/s11468-012-9470-1>
39. K. Kneipp, H. Kneipp, J. Kneipp, *Chem. Sci.* **6**(5), 2721 (2015). <https://doi.org/10.1039/C4SC03508A>
40. M.A. Boles, M. Engel, D.V. Talapin, *Chem. Rev.* **116**(18), 11220 (2016). <https://doi.org/10.1021/acs.chemrev.6b00196>
41. M. Grzelczak, L.M. Liz-Marzán, R. Klajn, *Chem. Soc. Rev.* **48**(5), 1342 (2019). <https://doi.org/10.1039/C8CS00787J>
42. S. Gwo, H.-Y. Chen, M.-H. Lin, L. Sun, X. Li, *Chem. Soc. Rev.* **45**(20), 5672 (2016). <https://doi.org/10.1039/C6CS00450D>
43. Y. Yao, Y. Li, X. Zeng, N. Sun, R. Sun, J.-B. Xu, C.-P. Wong, *J. Mater. Chem. A* **6**(14), 5984 (2018). <https://doi.org/10.1039/C8TA00310F>
44. A. Rai, S. Bhaskar, K.M. Ganesh, S.S. Ramamurthy, *ACS Appl. Nano Mater.* **5**(9), 12245 (2022). <https://doi.org/10.1021/acsanm.2c02556>
45. L. Liu, S. Bhaskar, B.T. Cunningham, *Appl. Phys. Lett.* **124**(23), 234101 (2024). <https://doi.org/10.1063/5.0203701>
46. N. Ganesh, P.C. Mathias, W. Zhang, B.T. Cunningham, *J. Appl. Phys.* **103**(8), 083104 (2008). <https://doi.org/10.1063/1.2906175>
47. P.C. Mathias, N. Ganesh, W. Zhang, B.T. Cunningham, *J. Appl. Phys.* **103**(9), 094320 (2008). <https://doi.org/10.1063/1.2917184>
48. S. Bhaskar, W. Liu, J. Tibbs, B.T. Cunningham, *Appl. Phys. Lett.* **124**(16), 161102 (2024). <https://doi.org/10.1063/5.0203999>
49. Z.-H. Chen, L. Li, H. Shi, Y. Wang, F. Sun, Y. Yang, *IEEE J. Sel. Top. Quantum Electron.* **27**(1), 5500107 (2021). <https://doi.org/10.1109/JSTQE.2020.3026446>
50. B. Shi, Z. Chen, Q. Wang, Q. Wang, D. Guo, Y. Wang, Z. Gan, *Opt. Laser Technol.* **177**, 111232 (2024). <https://doi.org/10.1016/j.optlastec.2024.111232>
51. J. Song, X. Liu, H. Xie, Y. Wang, Z. Gan, Z. Chen, *Opt. Laser Technol.* **179**, 111319 (2024). <https://doi.org/10.1016/j.optlastec.2024.111319>
52. D. Thacharakkal, S. Bhaskar, T. Sharma, G. Rajaraman, S. Sathish Ramamurthy, C. Subramaniam, *Chem. Eng. J.* **480**, 148166 (2023). <https://doi.org/10.1016/j.cej.2023.148166>
53. S.-H. Cao, W.-P. Cai, Q. Liu, Y.-Q. Li, *Annu. Rev. Anal. Chem.* **5**(1), 317 (2012). <https://doi.org/10.1146/annurev-anchem-062011-143208>
54. W. Xie, B. Walkenfort, S. Schlücker, *J. Am. Chem. Soc.* **135**(5), 1657 (2013). <https://doi.org/10.1021/ja309074a>
55. S. Dutta Choudhury, R. Badugu, J.R. Lakowicz, *Acc. Chem. Res.* **48**(8), 2171 (2015). <https://doi.org/10.1021/acs.accounts.5b00100>
56. S. Bhaskar, P. Das, V. Srinivasan, S.B.N. Bhaktha, S.S. Ramamurthy, *Mater. Res. Bull.* **145**, 111558 (2022). <https://doi.org/10.1016/j.materresbull.2021.111558>
57. S. Bhaskar, R. Dahiwadkar, S. Kanvah, S.S. Ramamurthy, S.B. Bn, *ACS Appl. Nano Mater.* **6**(20), 19312 (2023). <https://doi.org/10.1021/acsanm.3c03731>
58. M.H. Chowdhury, K. Ray, C.D. Geddes, J.R. Lakowicz, *Chem. Phys. Lett.* **452**(1), 162 (2008). <https://doi.org/10.1016/j.cplett.2007.12.047>
59. J. Turkevich, P.C. Stevenson, J. Hillier, *Discuss. Faraday Soc.* **11**, 55 (1951). <https://doi.org/10.1039/df9511100055>
60. S. Dutta Choudhury, R. Badugu, K. Ray, J.R. Lakowicz, *J. Phys. Chem. C* **117**(30), 15798 (2013). <https://doi.org/10.1021/jp4051066>
61. I. Gryczynski, J. Malicka, Z. Gryczynski, J.R. Lakowicz, *Anal. Biochem.* **324**(2), 170 (2004). <https://doi.org/10.1016/j.ab.2003.09.036>
62. V.S.K. Cheerala, K.M. Ganesh, S. Bhaskar, S.S. Ramamurthy, S.C. Neelakantan, *Langmuir* **39**(22), 7939 (2023). <https://doi.org/10.1021/acs.langmuir.3c00801>



63. D.S. Smith, Y. Kostov, G. Rao, *Appl. Opt.* **47**(28), 5229 (2008). <https://doi.org/10.1364/AO.47.005229>
64. L. Zhu, R. Badugu, D. Zhang, R. Wang, E. Descrovi, J.R. Lakowicz, *Anal. Biochem.* **531**, 20 (2017). <https://doi.org/10.1016/j.ab.2017.05.020>
65. K.M. Ganesh, S. Bhaskar, V.S.K. Cheerala, P. Battampara, R. Reddy, S.C. Neelakantan, N. Reddy, S.S. Ramamurthy, *Nanomaterials* (Basel) **14**(1), 111 (2024). <https://doi.org/10.3390/nano14010111>
66. S. Bhaskar, *Micromachines* (Basel) **14**(3), 574 (2023). <https://doi.org/10.3390/mi14030574>
67. K. Aslan, Z. Leonenko, J.R. Lakowicz, C.D. Geddes, *J. Fluoresc.* **15**(5), 643 (2005). <https://doi.org/10.1007/s10895-005-2970-z>
68. S.V. Boriskina, T.A. Cooper, L. Zeng, G. Ni, J.K. Tong, Y. Tsurimaki, Y. Huang, L. Meroueh, G. Mahan, G. Chen, *Adv. Opt. Photonics* **9**(4), 775 (2017). <https://doi.org/10.1364/AOP.9.000775>
69. J.B. Khurgin, *Nat. Nanotechnol.* **10**(1), 2 (2015). <https://doi.org/10.1038/nnano.2014.310>
70. S. Bhaskar, A.K. Singh, P. Das, P. Jana, S. Kanvah, B.N.S. Bhaktha, S.S. Ramamurthy, *ACS Appl. Mater. Interfaces* **12**(30), 34323 (2020). <https://doi.org/10.1021/acsami.0c07515>
71. Z. Li, *Adv. Opt. Mater.* **6**(16), 1701097 (2018). <https://doi.org/10.1002/adom.201701097>
72. W. Ahmed, İ.M. Öztürk, R.M.F. Iftikhar, A. Bek, *Mater. Chem. Phys.* **278**, 125589 (2022). <https://doi.org/10.1016/j.matchemphys.2021.125589>
73. H. Wang, N.J. Halas, *Adv. Mater.* **20**(4), 820 (2008). <https://doi.org/10.1002/adma.200701293>
74. S. Kim, S. Yoo, D.H. Nam, H. Kim, J.H. Hafner, S. Lee, *Nano Converg.* **11**(1), 26 (2024). <https://doi.org/10.1186/s40580-024-00435-4>
75. Fernández-Galiana, O. Bibikova, S. Vilms Pedersen, M.M. Stevens, *Adv. Mater.* **36**(43), 2210807 (2023). <https://doi.org/10.1002/adma.202210807>
76. P. Zhang, X. Zhou, S. Wang, *Chem. Methods* **3**(6), e202200066 (2023). <https://doi.org/10.1002/cmtd.202200066>
77. S. Bhaskar, S.S. Ramamurthy, "Performance Enhancement of Light Emitting Radiating Dipoles (LERDs) Using Surface Plasmon-Coupled and Photonic Crystal-Coupled Emission Platforms," in *Organic and Inorganic Light Emitting Diodes* (CRC Press, Boca Raton, 2023), chap. 8, p. 161
78. I.D. Block, P.C. Mathias, N. Ganesh, S.I. Jones, B.R. Dorvel, V. Chaudhery, L.O. Vodkin, R. Bashir, B.T. Cunningham, *Opt. Express* **17**(15), 13222 (2009). <https://doi.org/10.1364/OE.17.013222>
79. P.C. Mathias, H.-Y. Wu, B.T. Cunningham, *Appl. Phys. Lett.* **95**(2), 021111 (2009). <https://doi.org/10.1063/1.3184573>
80. A. Pokhriyal, M. Lu, C.S. Huang, S. Schulz, B.T. Cunningham, *Appl. Phys. Lett.* **97**(12), 121108 (2010). <https://doi.org/10.1063/1.3485672>
81. A. Pokhriyal, M. Lu, V. Chaudhery, S. George, B.T. Cunningham, *Appl. Phys. Lett.* **102**(22), 221114 (2013). <https://doi.org/10.1063/1.4809513>
82. J.R. Lakowicz (ed.), *Principles of Fluorescence Spectroscopy* (Springer, Boston, 2006). <https://doi.org/10.1007/978-0-387-46312-4>
83. M.H. Chowdhury, K. Ray, S.K. Gray, J. Pond, J.R. Lakowicz, *Anal. Chem.* **81**(4), 1397 (2009). <https://doi.org/10.1021/ac802118s>
84. H. Wang, H. Li, S. Xu, B. Zhao, W. Xu, *Sci. Rep.* **7**(1), 14630 (2017). <https://doi.org/10.1038/s41598-017-15111-3>
85. H. Lüder, M. Gerken, *Opt. Quantum Electron.* **51**(5), 139 (2019). <https://doi.org/10.1007/s11082-019-1838-4>
86. P. Gupta, *Plasmonics* (Norwell, Mass.) **13**(6), 2067 (2018). <https://doi.org/10.1007/s11468-018-0723-5>
87. D. Genovese, S. Bonacchi, R. Juris, M. Montalti, L. Prodi, E. Rampazzo, N. Zaccheroni, *Angew. Chem.* **52**, 5965 (2013)
88. G.C. Phan-Quang, X. Han, C.S.L. Koh, H.Y.F. Sim, C.L. Lay, S.X. Leong, Y.H. Lee, N. Pazos-Perez, R.A. Alvarez-Puebla, X.Y. Ling, *Acc. Chem. Res.* **52**(7), 1844 (2019). <https://doi.org/10.1021/acs.accounts.9b00163>
89. C. Dai, Z. Lin, K. Agarwal, C. Mikhael, A. Aich, K. Gupta, J.-H. Cho, *Nano Lett.* **20**(9), 6697 (2020). <https://doi.org/10.1021/acs.nanolett.0c02575>
90. S.R. Sahoo, C.-T. Huang, K. Tsai, G.-J. Wang, C.-C. Chang, *Appl. Phys. Rev.* **10**(4), 041403 (2023). <https://doi.org/10.1063/5.0155256>
91. S. Dutta Choudhury, R. Badugu, K. Nowaczyk, K. Ray, J.R. Lakowicz, *J. Phys. Chem. Lett.* **4**(1), 227 (2013). <https://doi.org/10.1021/jz301867b>
92. K.M. Ganesh, S.S.M. Lis, S.P. Nayak, P. Das, S. Bhaskar, N. Reddy, M.A. Hossain, C.B. Sanjeevi, S.S. Ramamurthy, B.N. Shivakiran Bhaktha, "Surface Plasmon Resonance Waveguides and Their Applications: Insights from Functional Metal–Dielectric–Metal Interfaces," in *Nano-Engineering at Functional Interfaces for Multi-Disciplinary Applications* (Elsevier, Amsterdam, 2025), chap. 5, pp. 93–121. <https://doi.org/10.1016/B978-0-443-21691-6.00006-8>
93. R. Badugu, E. Descrovi, J.R. Lakowicz, *Anal. Biochem.* **445**, 1 (2014). <https://doi.org/10.1016/j.ab.2013.10.009>
94. Y. Wu, P. Xie, Q. Ding, Y. Li, L. Yue, H. Zhang, W. Wang, *J. Appl. Phys.* **133**(3), 030902 (2023). <https://doi.org/10.1063/5.0131903>
95. A. Gabbani, G. Petrucci, F. Pineider, *J. Appl. Phys.* **129**(21), 211101 (2021). <https://doi.org/10.1063/5.0050034>
96. I.S. Maksymov, *Rev. Phys.* **1**, 36 (2016). <https://doi.org/10.1016/j.revip.2016.03.002>
97. J.B. Pendry, A.J. Holden, D.J. Robbins, W.J. Stewart, *IEEE Trans. Microwave Theory Techn.* **47**(11), 2075 (1999). <https://doi.org/10.1109/22.798002>
98. P. Wang, J. Huh, J. Lee, K. Kim, K.J. Park, S. Lee, Y. Ke, *Adv. Mater.* **31**(29), 1901364 (2019). <https://doi.org/10.1002/adma.201901364>
99. J.A. Fan, C. Wu, K. Bao, J. Bao, R. Bardhan, N.J. Halas, V.N. Manoharan, P. Nordlander, G. Shvets, F. Capasso, *Science* **328**(5982), 1135 (2010). <https://doi.org/10.1126/science.1187949>
100. A. Nazir, S. Panaro, R. Proietti Zaccaria, C. Liberale, F. De Angelis, A. Toma, *Nano Lett.* **14**(6), 3166 (2014). <https://doi.org/10.1021/nl500452p>
101. F. Shafiei, F. Monticone, K.Q. Le, X.-X. Liu, T. Hartsfield, A. Alù, X. Li, *Nat. Nanotech* **8**(2), 95 (2013). <https://doi.org/10.1038/nnano.2012.249>
102. S. Panaro, A. Nazir, R. Proietti Zaccaria, L. Razzari, C. Liberale, F. De Angelis, A. Toma, *Nano Lett.* **15**(9), 6128 (2015). <https://doi.org/10.1021/acs.nanolett.5b02407>
103. J.R. Lakowicz, *Anal. Biochem.* **337**(2), 171 (2005). <https://doi.org/10.1016/j.ab.2004.11.026>
104. J.R. Lakowicz, *Anal. Biochem.* **298**(1), 1 (2001). <https://doi.org/10.1006/abio.2001.5377>
105. J.R. Lakowicz, Y. Shen, S. D'Auria, J. Malicka, J. Fang, Z. Gryczynski, I. Gryczynski, *Anal. Biochem.* **301**(2), 261 (2002). <https://doi.org/10.1006/abio.2001.5503>
106. J.R. Lakowicz, *Anal. Biochem.* **324**(2), 153 (2004). <https://doi.org/10.1016/j.ab.2003.09.039>
107. R. Badugu, K. Nowaczyk, E. Descrovi, J.R. Lakowicz, *Anal. Biochem.* **442**(1), 83 (2013). <https://doi.org/10.1016/j.ab.2013.07.021>
108. S. Bhaskar, K.M. Ganesh, D. Arora, Y. Gupta, B.G. Maddala, A. Bonyár, W. Tawfik, S.S. Ramamurthy, N.S.V. Kambhampati, "Nanoengineering at Functional Plasmonic Interfaces," in *Nano-Engineering at Functional Interfaces for Multi-Disciplinary Applications* (Elsevier, Amsterdam, 2025), chap. 3, pp. 47–73. <https://doi.org/10.1016/B978-0-443-21691-6.00004-4>
109. S.S. Ramamurthy, S. Bhaskar, N. Reddy (eds.), *Nano-Engineering at Functional Interfaces for Multi-Disciplinary Applications* (Elsevier, Amsterdam, 2025). <https://doi.org/10.1016/C2023-0-00018-8>
110. S. Bhaskar, P. Jha, C. Subramaniam, S.S. Ramamurthy, *Physica E Low Dimens. Syst. Nanostruct.* **132**, 114764 (2021). <https://doi.org/10.1016/j.physe.2021.114764>
111. A. Rai, S. Bhaskar, N. Reddy, S.S. Ramamurthy, *ACS Sustain. Chem. Eng.* **9**(44), 14959 (2021). <https://doi.org/10.1021/acssuschemeng.1c05437> □

Publisher's note

Springer Nature remains neutral with regard to jurisdictional claims in published maps and institutional affiliations.

Springer Nature or its licensor (e.g. a society or other partner) holds exclusive rights to this article under a publishing agreement with the author(s) or other rightsholder(s); author self-archiving of the accepted manuscript version of this article is solely governed by the terms of such publishing agreement and applicable law.